remote sensing

Article

Calibration Method of Array Errors for Wideband MIMO Imaging Radar Based on Multiple Prominent Targets

Zheng Zhao [1], Weiming Tian [2,3], Yunkai Deng [1,*], Cheng Hu [1,4] and Tao Zeng [1,2]

1 Radar Research Lab, School of Information and Electronics, Beijing Institute of Technology, Beijing 100081, China; 3120185426@bit.edu.cn (Z.Z.); cchchb@bit.edu.cn (C.H.); zengtao@bit.edu.cn (T.Z.)
2 Key Laboratory of Electronics and Information Technology in Satellite Navigation, Beijing Institute of Technology, Ministry of Education, Beijing 100081, China; tianweiming@bit.edu.cn
3 Beijing Institute of Technology Chongqing Innovation Center, Chongqing 401120, China
4 Advanced Technology Research Institute, Beijing Institute of Technology, Jinan 250300, China
* Correspondence: yunkai_bit@bit.edu.cn; Tel.: +86-010-6891-8043

Abstract: Wideband multiple-input-multiple-output (MIMO) imaging radar can achieve high-resolution imaging with a specific multi-antenna structure. However, its imaging performance is severely affected by the array errors, including the inter-channel errors and the position errors of all the transmitting and receiving elements (TEs/REs). Conventional calibration methods are suitable for the narrow-band signal model, and cannot separate the element position errors from the array errors. This paper proposes a method for estimating and compensating the array errors of wideband MIMO imaging radar based on multiple prominent targets. Firstly, a high-precision target position estimation method is proposed to acquire the prominent targets' positions without other equipment. Secondly, the inter-channel amplitude and delay errors are estimated by solving an equation-constrained least square problem. After this, the element position errors are estimated with the genetic algorithm to eliminate the spatial-variant error phase. Finally, the feasibility and correctness of this method are validated with both simulated and experimental datasets.

Keywords: MIMO imaging radar; array error calibration; inter-channel error; element position error; prominent target

check for updates

Citation: Zhao, Z.; Tian, W.; Deng, Y.; Hu, C.; Zeng, T. Calibration Method of Array Errors for Wideband MIMO Imaging Radar Based on Multiple Prominent Targets. *Remote Sens.* **2021**, *13*, 2997. https://doi.org/10.3390/rs13152997

Academic Editors: Lei Zhang and Zhong Lu

Received: 18 June 2021
Accepted: 28 July 2021
Published: 30 July 2021

Publisher's Note: MDPI stays neutral with regard to jurisdictional claims in published maps and institutional affiliations.

Copyright: © 2021 by the authors. Licensee MDPI, Basel, Switzerland. This article is an open access article distributed under the terms and conditions of the Creative Commons Attribution (CC BY) license (https://creativecommons.org/licenses/by/4.0/).

1. Introduction

Landslide events are one of the most typical and frequent geological phenomena. Surface deformations normally occur before the macro failure of natural and engineered slopes. Deformation measurement is of great significance to monitor and forecast landslide events. Ground-based synthetic aperture radar (GB-SAR) has been widely utilized to measure the surface deformation of large-scale scenes, with the advantages of being all-day, all-weather, non-contacting, and highly accurate [1,2]. Generic GB-SAR systems acquire a large aperture based on the mechanical movement of the transmitting and receiving (T/R) antennas along a rail track. A novel and equivalent measuring tool with traditional GB-SAR, i.e., multiple-input-multiple-output (MIMO) radar, has been developed [3,4].

MIMO radar, featured with a multi-antenna structure including transmitting and receiving arrays, is a state-of-the-art technique in radar applications. Utilizing a small number of actual T/R antennas, it can be equivalent to a rather large number of observation channels. MIMO radar uses the waveform diversity technique to synthesize a large aperture, which is the largest difference to a generic GB-SAR. To acquire good range resolution, MIMO radar typically transmits wideband signal. It should be noted that the GB-MIMO radar discussed in this paper is an imaging radar system. Different from tracking MIMO or array radar, the main advantages of GB-MIMO radar are focused on its fast image acquisition and good image resolution, which has shown great application potential in deformation monitoring, weak vibration measurement and other typical InSAR (interferometric synthetic aperture radar) applications [5,6].

Due to the specific multi-antenna structure of MIMO radar, different types of array errors are inevitable in its practical use, mainly including element position error and inter-channel error [7,8]. These errors affect the designed performance of the system and defocus image results, thus affecting the subsequent InSAR applications. The first type is caused by mechanical working accuracy or structural distortion of the array panel and antennas, causing the actual positions of T/R elements to slightly deviate from their theoretical design positions. Although position errors are on the milli- or sub-millimeter level, the phase errors caused by the position errors cannot be ignored. Relevant research prove that these phase errors are spatially variant, which means that phase errors for targets with different azimuths are different [9,10]. The second type of error is specific to MIMO radar. Since the radar hardware, including amplifiers, transmission lines, and electronic switches, are independent between different T/R channels, the echo's amplification, delay and phase modulation are also slightly inconsistent [11].

The calibration methods of array errors have been widely studied and can be mainly divided into two types, including the active calibration method and the self-calibration method [12–15]. The first type demands some reference targets whose positions are known, while the second type usually constructs a cost function according to an optimization criterion, and then iteratively estimates the array errors. Although some methods are useful for traditional searching MIMO, they cannot be directly used for wideband imaging MIMO. Firstly, the phase-only calibration method is invalid due to the narrow-band assumption and the theoretical basis of array steering vectors [16,17]. Secondly, the conventional methods do not distinguish the inter- and position-errors [18]. The spatial-varying errors can only be compensated in a small scale or be averaged through the whole image. None can achieve good estimation with both wide-coverage and high-precision.

A method proposed in [19] estimates the inter-channel amplitude and phase errors based on a single prominent target. By adjusting the weights of all channels, errors between the azimuth imaging result and the ideal result of this prominent target are minimized with a least square error method. However, this method can only estimate the inter-channel errors. Another method is proposed in [20] to calibrate the amplitude and phase errors of intra- and inter-channels for near-field MIMO radar. Utilizing multiple prominent targets whose positions are known, the total energy of these targets' sidelobes is minimized based on a criterion that the peaks of all the targets reach ideal levels. However, this method ignores the spatial variation caused by the element position errors, and good focus performances for targets over the whole image cannot be guaranteed.

In order to solve those problems above, a high-precision estimation and calibration method of array errors based on multiple prominent targets is proposed. Firstly, a multi-target position joint estimation method is proposed to estimate prominent targets' coordinates without other equipment. Secondly, the inter-channel amplitude and delay errors are compensated by solving an equation-constrained least square problem. After this, the element position errors are estimated to eliminate the residual phase error. Finally, a numerical simulation and a field experiment are performed. The processing results prove that with the proposed method, the imaging performance of the wideband MIMO radar can be significantly improved.

2. Modeling and Analysis of Array Errors

2.1. Error Classification and Echo Modeling

For a MIMO radar system, its performance is severely affected by the array errors, which can be mainly divided into two types: inter-channel errors and element position errors. As shown in Figure 1, the inter-channel errors are mainly caused by the inconsistency of the amplitude, phase and delay characteristics of different channels. The element position errors are mainly caused by the limitation of mechanical working accuracy, which further affect the phase center of the array.

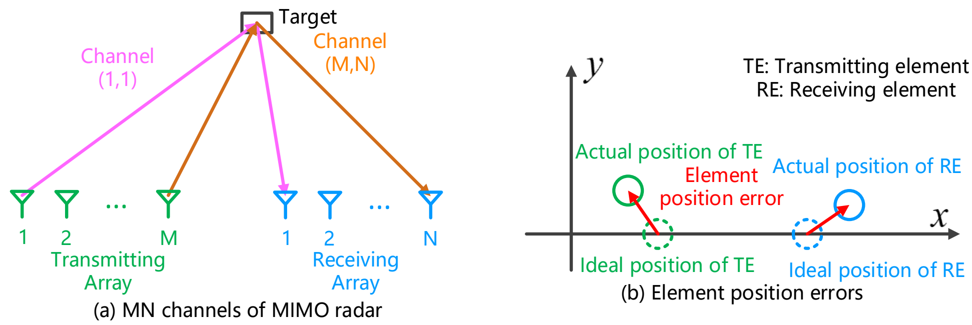

Figure 1. Array errors of MIMO imaging radar.

As shown in Figure 2, the geometric center of the transmitting array is used as the coordinate origin, the line along the transmitting array is used as the y axis, and the target P is located in the positive direction of the x axis. Because of the element position errors, the TEs are not completely collinear. It is assumed that the coordinates of all the TEs and REs are $(\tilde{x}_{T,m}, \tilde{y}_{T,m}), m = 1, 2, \ldots, M$ and $(\tilde{x}_{R,n}, \tilde{y}_{R,n}), n = 1, 2, \ldots, N$, respectively.

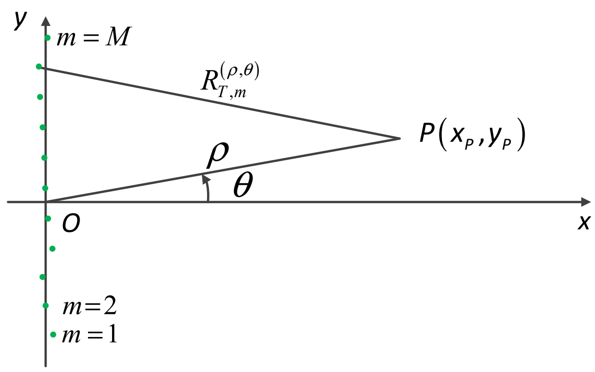

Figure 2. Schematic diagram of a target and an array.

The target P is located at (x_P, y_P) in the Cartesian coordinate system, and at (ρ, θ) in the polar coordinate system. The following condition is satisfied

$$\begin{cases} \rho = \sqrt{x_P^2 + y_P^2} \\ \theta = \arctan(y_P/x_P) \end{cases}. \tag{1}$$

From this, the echo of the target P for the channel (m, n) can be expressed as:

$$\tilde{s}_r(t, m, n; \rho, \theta) = A_{T,m} A_{R,n} \sigma(\rho, \theta) \exp[j(\phi_{T,m} + \phi_{R,n})] s\left(t - \frac{\tilde{R}_{T,m}^P + \tilde{R}_{R,n}^P}{c} - \Delta\tau_{T,m} - \Delta\tau_{R,n}\right) \tag{2}$$

where $\sigma(\rho, \theta)$ is the complex scattering coefficient; $A_{T,m}$, $\phi_{T,m}$ and $\Delta\tau_{T,m}$ are the amplitude, phase and delay error of the mth TE; and $A_{R,n}$, $\phi_{R,n}$ and $\Delta\tau_{R,n}$ are the amplitude, phase and delay error of the nth RE, respectively. $\tilde{R}_{T,m}^P$ and $\tilde{R}_{R,n}^P$ are the distances from P to the mth TE and the nth RE, including the element position errors.

After pulse compression, the echo can be expressed as:

$$\begin{aligned} \tilde{s}_{mf}(t, m, n; \rho, \theta) &= A_{T,m} A_{R,n} \sigma(\rho, \theta) \cdot \exp(j(\phi_{T,m} + \phi_{R,n})) \\ &\cdot sinc\left[B\left(t - \left(\frac{\tilde{R}_{T,m}^P + \tilde{R}_{R,n}^P}{c} + \Delta\tau_{T,m} + \Delta\tau_{R,n}\right)\right)\right] \exp\left(-j\frac{2\pi}{\lambda}\left(\tilde{R}_{T,m}^P + \tilde{R}_{R,n}^P + \Delta\tau_{T,m} c + \Delta\tau_{R,n} c\right)\right) \end{aligned} \tag{3}$$

where B is the signal bandwidth.

In far-field condition, with 1st-order Taylor expansion of $\widetilde{R}^{p}_{T,m}$ and $\widetilde{R}^{p}_{R,n}$, the element position error can be expressed as:

$$\begin{aligned}
&\widetilde{s}_{mf}(t,m,n;\rho,\theta) \\
&\approx \underbrace{A_{T,m}A_{R,n}}_{Amplitude}\sigma(\rho,\theta)\exp\Big(j\Big(\underbrace{\phi_{T,m}+\phi_{R,n}-\tfrac{2\pi(\Delta\tau_{T,m}c+\Delta\tau_{R,n}c)}{\lambda}}_{Phase\ induced\ by\ Channel}\Big)\Big) \\
&\cdot sinc\Big[B\Big(t-\underbrace{\Big(\tfrac{2\rho-(\widetilde{x}_{T,m}+\widetilde{x}_{R,n})\cos\theta-(\widetilde{y}_{T,m}+\widetilde{y}_{R,n})\sin\theta}{c}+\Delta\tau_{T,m}+\Delta\tau_{R,n}\Big)}_{Envelope}\Big)\Big] \\
&\cdot\exp\underbrace{\{-j\tfrac{2\pi}{\lambda}[2\rho-(\widetilde{x}_{T,m}+\widetilde{x}_{R,n})\cos\theta-(\widetilde{y}_{T,m}+\widetilde{y}_{R,n})\sin\theta]\}}_{Phase\ induced\ by\ Transmission\ Path}
\end{aligned} \tag{4}$$

Inter-channel errors, including $A_{T,m}$, $A_{R,n}$, $\phi_{T,m}$, $\phi_{R,n}$, $\Delta\tau_{T,m}$, and $\Delta\tau_{R,n}$, belong to systemic errors and are independent of the target's position (ρ,θ). Thus, the first two terms of (4) are spatially invariant. The phase term induced by the transmission path is affected by the element position error, and changes with the target's azimuth θ. Besides, the inter-channel delay errors $\Delta\tau_{T,m}$ and $\Delta\tau_{R,n}$ not only affect the phase induced by the channel, but also the signal envelope after pulse compression. For a wideband MIMO radar, the internal delay characteristics may cause a shift comparable to the range resolution.

2.2. Characteristics of Element Position Error

Assuming that the inter-channel errors can be completely eliminated, (4) can be simplified as:

$$\begin{aligned}
\widetilde{s}_{mf}(t,m,n;\rho,\theta) &= \sigma(\rho,\theta)\mathrm{sinc}\Big[B\Big(t-\tfrac{2\rho-(\widetilde{x}_{T,m}+\widetilde{x}_{R,n})\cos\theta-(\widetilde{y}_{T,m}+\widetilde{y}_{R,n})\sin\theta}{c}\Big)\Big] \\
&\cdot\exp\{-j\tfrac{2\pi}{\lambda}[2\rho-(\widetilde{x}_{T,m}+\widetilde{x}_{R,n})\cos\theta-(\widetilde{y}_{T,m}+\widetilde{y}_{R,n})\sin\theta]\}
\end{aligned} \tag{5}$$

Since the element position errors are far smaller than the radar range resolution, the offset of the 'sinc' peak caused by the element position errors can be negligible. When taking the azimuth focusing with the back-projection (BP) algorithm [21], the echoes should be compensated according to the target's range history. The compensated phase is calculated based on the ideal element position $y_{T,m}$ and $y_{R,n}$:

$$\phi_{ref}(m,n;\rho,\theta) = -\frac{2\pi}{\lambda}[2\rho-(y_{T,m}+y_{R,n})\sin\theta] \tag{6}$$

Therefore, the residual phase of each channel can be expressed as

$$\Delta\phi_{mf}(m,n;\rho,\theta) \approx \frac{2\pi}{\lambda}(\Delta x_{T,m}\cos\theta+\Delta y_{T,m}\sin\theta)+\frac{2\pi}{\lambda}(\Delta x_{R,n}\cos\theta+\Delta y_{R,n}\sin\theta) \tag{7}$$

where $\Delta x_{T,m}$, $\Delta y_{T,m}$, $\Delta x_{R,n}$ and $\Delta y_{R,n}$ are the 2D element errors of the MIMO system. The residual phase errors are proportional to the element position errors. If the element position error cannot be well compensated, a severe grating lobe problem would be caused.

3. Array Errors Calibration Based on Multiple Prominent Targets

3.1. Position Estimation of Prominent Targets

As shown in Figure 3, K prominent targets $\{P_k|k=1,2,\ldots,K\}$ are placed at K different azimuths in the far field. Since it is necessary to extract the peaks' phase of each target in each channel, it should be ensured that the main-lobes of any two prominent targets after pulse compression are separated. A high-precision position estimation method of multi-point targets is proposed. In order to accurately estimate the position (ρ_k,θ_k) of each prominent target in the polar coordinate as shown in Figure 2, a three-step method is adopted, including relative azimuth angle estimation, reference angle estimation and range estimation.

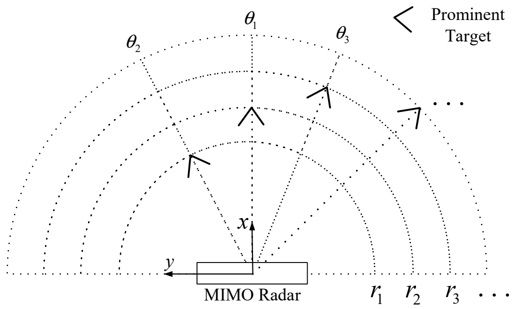

Figure 3. Sketch map of the prominent targets.

Firstly, the MIMO radar transmits and receives the wideband signals. After taking pulse compression, MN channels of compressed signals can be obtained. After, K peaks corresponding to every prominent target for each channel are extracted. From (4), the phase components of the $(m,n)^{th}$ peak of a prominent target can be expressed as

$$\begin{array}{l}\Phi\left\{s_{mf}(m,n;\rho,\theta)\right\} \\ = \langle\sigma(\rho,\theta)\rangle + \phi_{T,m} + \phi_{R,n} - \frac{2\pi(\Delta\tau_{T,m}c+\Delta\tau_{R,n}c)}{\lambda} \\ -\frac{2\pi}{\lambda}[2\rho - (\tilde{x}_{T,m}+\tilde{x}_{R,n})\cos\theta - (\tilde{y}_{T,m}+\tilde{y}_{R,n})\sin\theta]\end{array} \tag{8}$$

A cancellation is firstly operated between two prominent targets' peak signals to eliminate the inter-channel errors. It can be obtained as,

$$\begin{aligned}\Phi_d(m,n) &= \Phi\left\{s_{mf}(m,n;\rho_1,\theta_1)\right\} - \Phi\left\{s_{mf}(m,n;\rho_2,\theta_2)\right\} \\ &= \langle\sigma(\rho_1,\theta_1)\rangle - \langle\sigma(\rho_2,\theta_2)\rangle - \frac{2\pi}{\lambda}\left(\begin{array}{l}2(\rho_1-\rho_2) \\ -(\tilde{x}_{T,m}+\tilde{x}_{R,n})(\cos\theta_1-\cos\theta_2) \\ -(\tilde{y}_{T,m}+\tilde{y}_{R,n})(\sin\theta_1-\sin\theta_2)\end{array}\right)\end{aligned} \tag{9}$$

After, another cancellation between any two adjacent channels is further operated,

$$\begin{aligned}\Phi_{dd}(m,n) &= \Phi_d(m+1,n) - \Phi_d(m,n) \\ &= \frac{2\pi}{\lambda}(\cos\theta_1-\cos\theta_2)(\Delta x_{T,m+1}-\Delta x_{T,m}) \\ &\quad -\frac{2\pi}{\lambda}(\sin\theta_1-\sin\theta_2)(\Delta y_{T,m+1}-\Delta y_{T,m}) - \frac{2\pi d}{\lambda}(\sin\theta_1-\sin\theta_2)\end{aligned} \tag{10}$$

where d is the interval of the virtual array of the MIMO system. For a wideband MIMO imaging radar, d is usually designed to be a constant of $\lambda/2$ [22,23].

Considering that the expectation of the element position error is almost zero, the relative azimuth angle of any two prominent targets can be acquired through the two-step cancellation data,

$$\sin\theta_1 - \sin\theta_2 = \frac{E[\Phi_{dd}(m,n)]}{-\pi}. \tag{11}$$

where $E[\,]$ denotes the expectation operation.

Secondly, a reference angle $\hat{\theta}_1$ of the first target is estimated to get these prominent targets' exact azimuth angles. According to the peak locations of each channel of compressed signal, the peak range of the kth target for the MN channels, $R_{k,m,n}$, can also be acquired. Since the angle deviation would cause a variance increment of the range history $R_{k,m,n}$ of each target, $\hat{\theta}_1$ is estimated by finding the minimum value of the below equation:

$$\hat{\theta}_1 = \arg_{\theta_1}\left(\min\left(\sum_{k=1}^{K}\mathrm{var}(R_{k,m,n} - (y_{T,m}+y_{R,n})\sin(\theta_1+\vartheta_k))\right)\right) \tag{12}$$

where ϑ_k is the relative angle between the kth and first targets, and can be calculated from (11).

Finally, the range coordinate ρ of each prominent target is estimated. The basic strategy of range estimation is the same with that of azimuth estimation. According to (4), the range history of the kth target in every channel can be expressed as

$$R_{k,m,n} = 2\rho_k - (y_{T,m} + y_{R,n})\sin(\theta_k) + c(\Delta\tau_{T,m} + \Delta\tau_{R,n}) + \varepsilon \tag{13}$$

It should be noted that the range error caused by the element position error is expressed as a random noise ε since it is relatively small. θ_k has been acquired in (11) and (12), so the second term of (13) can be calculated. The third term is independent of different targets and can be eliminated by a cancelation between two targets' peaks in every same channel. Thus, the relative range p_k between two targets can be expressed as

$$p_k = \rho_k - \rho_1 = \frac{E[R_{k,m,n} + (y_{T,m} + y_{R,n})\sin(\theta_k) - R_{1,m,n} - (y_{T,m} + y_{R,n})\sin(\theta_1)]}{2} \tag{14}$$

The reference range $\hat{\rho}_1$ of the first target can be estimated by LS (least-squares) optimization as below.

$$\hat{\rho}_1 = \arg_{\rho_1}\left(\min\left(\sum_k \frac{\sum_{m,n}(R_{k,m,n} - 2(\rho_1 + p_k) - (y_{T,m} + y_{R,n})\sin(\theta_k))^2}{MN}\right)\right) \tag{15}$$

Combined with the relative angle estimation in (11) and the reference angle estimation in (12), each target's angle can be acquired as $\theta_k = \hat{\theta}_1 + \vartheta_k$. Similarly, combined with the relative range estimation in (14) and the reference range estimation in (15), each target's range can be acquired as $\rho_k = \hat{\rho}_1 + p_k$.

3.2. Amplitude and Delay Error Estimation

3.2.1. Amplitude Error Estimation

As mentioned in Section 2, the amplitude and delay errors would not cause spatially variant phase errors. The peak amplitude $A_k(m,n)$ of the (m, n)th channel of the kth prominent target in (4) can be expressed as

$$\log(A_k(m,n)) = \log(A_{T.m}) + \log(A_{R.n}) + \log(|\sigma_k|) \tag{16}$$

Express all the equations in a matrix form (total $k(MN-1)$ equations) as

$$\log\begin{bmatrix} \mathbf{A}_1 \\ \mathbf{A}_2 \\ \vdots \\ \mathbf{A_k} \end{bmatrix} = \begin{bmatrix} \mathbf{G} \\ \mathbf{G} \\ \vdots \\ \mathbf{G} \end{bmatrix} \cdot \log\begin{bmatrix} \mathbf{A_T} \\ \mathbf{A_R} \end{bmatrix} \tag{17}$$

where

$$\begin{aligned} \mathbf{A_k} &= \begin{bmatrix} \frac{A_k(2,1)}{A_k(1,1)}, \cdots, \frac{A_k(M,1)}{A_k(1,1)}, \frac{A_k(1,2)}{A_k(1,1)}, \cdots \frac{A_k(1,M)}{A_k(1,1)}, & \cdots & , \frac{A_k(M,N)}{A_k(1,1)} \end{bmatrix}^T \in \mathbb{R}^{(MN-1)\times 1} \\ \mathbf{A_T} &= \begin{bmatrix} A^c_{T,1} & A^c_{T,2} & \cdots & A^c_{T,M} \end{bmatrix}^T \in \mathbb{R}^{M\times 1} \\ \mathbf{A_R} &= \begin{bmatrix} A^c_{R,1} & A^c_{R,2} & \cdots & A^c_{R,N} \end{bmatrix}^T \in \mathbb{R}^{N\times 1} \end{aligned} \tag{18}$$

and

$$\mathbf{G} = \begin{bmatrix} 0 & 0 & \cdots & 0 & -1 & 1 & \cdots & 0 \\ \vdots & \vdots & \ddots & \vdots & \vdots & \vdots & \ddots & \vdots \\ 0 & 0 & \cdots & 0 & -1 & 0 & \cdots & 1 \\ & & \vdots & & & \vdots & & \\ -1 & 0 & \cdots & 1 & 0 & 0 & \cdots & 0 \\ -1 & 0 & \cdots & 1 & -1 & 1 & \cdots & 0 \\ \vdots & \vdots & \ddots & \vdots & \vdots & \vdots & \ddots & \vdots \\ -1 & 0 & \cdots & 1 & -1 & 0 & \cdots & 1 \end{bmatrix} \in \mathbb{R}^{(MN-1)\times(M+N)} \tag{19}$$

Although the equation number is much bigger than the variables number, (17) is a rank-deficient equation set, whose rank is $M+N-2$. Two more constraints can be added as

$$\begin{bmatrix} 1 & 0_{(M-1)\times 1} & 0 & 0_{(N-1)\times 1} \\ 1 & 0_{(M-1)\times 1} & -1 & 0_{(N-1)\times 1} \end{bmatrix} \cdot \log \begin{bmatrix} \mathbf{A_T} \\ \mathbf{A_R} \end{bmatrix} = \mathbf{L} \cdot \log \begin{bmatrix} \mathbf{A_T} \\ \mathbf{A_R} \end{bmatrix} = 0 \tag{20}$$

From this, (17) turns into an equation-constrained least square problem (ECLS).

$$\min_{\mathbf{A_T A_R}} \left\| \log \begin{bmatrix} \mathbf{A}_1 \\ \vdots \\ \mathbf{A_k} \end{bmatrix} - \begin{bmatrix} \mathbf{G} \\ \vdots \\ \mathbf{G} \end{bmatrix} \cdot \log \begin{bmatrix} \mathbf{A_T} \\ \mathbf{A_R} \end{bmatrix} \right\|_2 \quad s.t.\ \mathbf{L} \cdot \log \begin{bmatrix} \mathbf{A_T} \\ \mathbf{A_R} \end{bmatrix} = 0 \tag{21}$$

According to [24], the closed solution can be obtained as:

$$\log \begin{bmatrix} \hat{\mathbf{A}}_\mathbf{T} \\ \hat{\mathbf{A}}_\mathbf{R} \end{bmatrix} = \left[\begin{bmatrix} \mathbf{G} \\ \vdots \\ \mathbf{G} \end{bmatrix} \cdot \left(\mathbf{I} - \mathbf{L}^\dagger \cdot \mathbf{L} \right) \right]^\dagger \cdot \log \begin{bmatrix} \mathbf{A}_1 \\ \vdots \\ \mathbf{A_k} \end{bmatrix} \tag{22}$$

where **I** is the unit matrix, and † represents the Moore–Penrose inverse.

3.2.2. Delay Error Estimation

As for the delay error, the ECLS method can also be used to estimate it. It has good consistency for different targets. The delay error can be compensated in MN equivalent channels independently instead of M+N transmitting and receiving channels. Utilizing the peak range $R_{k,m,n}$ of the (m, n)th channel, and the estimated range and azimuth (ρ_k, θ_k) of the kth target, the delay error $\hat{R}_i$ for each channel is estimated with an average operation:

$$\hat{R}_i = \frac{\sum_k [R_{k,m,n} - (y_{T,m} + y_{R,n}) \sin\theta_k - 2\rho_k]}{k}, i = 1, 2, \cdots, MN \tag{23}$$

3.3. Estimation of Element Position Errors

According to (10), the residual phase after average removal can be written as follows:

$$\begin{cases} \Delta\Phi(m,n) = \frac{2\pi}{\lambda}(\cos\theta_1 - \cos\theta_2)(\Delta x_{T,m+1} - \Delta x_{T,m}) - \frac{2\pi}{\lambda}(\sin\theta_1 - \sin\theta_2)(\Delta y_{T,m+1} - \Delta y_{T,m}) \\ \quad \textit{when RE is not switching} \\ \Delta\Phi(m,n) = \frac{2\pi}{\lambda}(\cos\theta_1 - \cos\theta_2)(\Delta x_{T,1} - \Delta x_{T,M}) - \frac{2\pi}{\lambda}(\sin\theta_1 - \sin\theta_2)(\Delta y_{T,1} - \Delta y_{T,M}) \\ \quad + \frac{2\pi}{\lambda}(\cos\theta_1 - \cos\theta_2)(\Delta x_{R,n+1} - \Delta x_{R,n}) - \frac{2\pi}{\lambda}(\cos\theta_1 - \cos\theta_2)(\Delta x_{R,n+1} - \Delta x_{R,n}) \\ \quad \textit{when RE is switching} \end{cases} \tag{24}$$

(24) is utilized to extract the element position errors by the cancellation between different targets in the same channel and build an equation set to estimate the 2D element position errors.

It was assumed that two prominent targets located at θ_1 and θ_2 are a group, and $s_{12} = \sin\theta_1 - \sin\theta_2$, $c_{12} = \cos\theta_1 - \cos\theta_2$.

$$\begin{cases} \mathbf{\Delta x_T} = [\Delta x_{T,1}, \ldots, \Delta x_{T,M}]^T \\ \mathbf{\Delta y_T} = [\Delta y_{T,1}, \ldots, \Delta y_{T,M}]^T \\ \mathbf{\Delta x_R} = [\Delta x_{R,1}, \ldots, \Delta x_{R,N}]^T \\ \mathbf{\Delta y_R} = [\Delta y_{R,1}, \ldots, \Delta y_{R,N}]^T \end{cases} \tag{25}$$

From this, a linear equation set can be obtained as follows:

$$\mathbf{\Delta\Phi}_{12}\mathbf{=}\mathbf{H}_{12}\mathbf{\Delta p_{TR}} \tag{26}$$

where

$$\mathbf{H}_{12} = \frac{2\pi}{\lambda}\left[\begin{array}{cccccccccccccccc}
0 & 0 & \cdots & 0 & 0 & 0 & \cdots & 0 & -c_{12} & c_{12} & \cdots & 0 & -s_{12} & s_{12} & \cdots & 0 \\
\vdots & \vdots & \ddots & \vdots & \vdots & \vdots & \ddots & \vdots & \vdots & \vdots & \ddots & \vdots & \vdots & \vdots & \ddots & \vdots \\
0 & 0 & \cdots & 0 & 0 & 0 & \cdots & 0 & 0 & \cdots & -c_{12} & c_{12} & 0 & \cdots & -s_{12} & s_{12} \\
-c_{12} & c_{12} & \cdots & 0 & -s_{12} & s_{12} & \cdots & 0 & c_{12} & 0 & \cdots & -c_{12} & s_{12} & 0 & \cdots & -s_{12} \\
0 & 0 & \cdots & 0 & 0 & 0 & \cdots & 0 & -c_{12} & c_{12} & \cdots & 0 & -s_{12} & s_{12} & \cdots & 0 \\
\vdots & \vdots & \ddots & \vdots & \vdots & \vdots & \ddots & \vdots & \vdots & \vdots & \ddots & \vdots & \vdots & \vdots & \ddots & \vdots \\
0 & 0 & \cdots & 0 & 0 & 0 & \cdots & 0 & 0 & \cdots & -c_{12} & c_{12} & 0 & \cdots & -s_{12} & s_{12} \\
 & \vdots & & & & \vdots & & & & \vdots & & & & \vdots & & \\
0 & \cdots & -c_{12} & c_{12} & 0 & \cdots & -s_{12} & s_{12} & c_{12} & 0 & \cdots & -c_{12} & s_{12} & 0 & \cdots & -s_{12} \\
0 & 0 & \cdots & 0 & 0 & 0 & \cdots & 0 & -c_{12} & c_{12} & \cdots & 0 & -s_{12} & s_{12} & \cdots & 0 \\
\vdots & \vdots & \ddots & \vdots & \vdots & \vdots & \ddots & \vdots & \vdots & \vdots & \ddots & \vdots & \vdots & \vdots & \ddots & \vdots \\
0 & 0 & \cdots & 0 & 0 & 0 & \cdots & 0 & 0 & \cdots & -c_{12} & c_{12} & 0 & \cdots & -s_{12} & s_{12}
\end{array}\right] \in \mathbb{R}^{(MN-1)\times(2M+2N)} \tag{27}$$

$$\mathbf{\Delta p_{TR}} = \begin{bmatrix} \mathbf{\Delta x_R^T} & \mathbf{\Delta y_R^T} & \mathbf{\Delta x_T^T} & \mathbf{\Delta y_T^T} \end{bmatrix}^T \in \mathbb{R}^{(2M+2N)\times 1}$$

According to (23), any two prominent targets can construct $MN - 1$ observation equations. Thus, at least three targets are needed to estimate the element position errors. With K prominent targets, a new equation set can be obtained as

$$\begin{aligned} \mathbf{\Delta\Phi} \quad &= \mathbf{H\Delta p_{TR}} \\ \begin{bmatrix} \mathbf{\Delta\Phi}_{12} \\ \mathbf{\Delta\Phi}_{23} \\ \vdots \\ \mathbf{\Delta\Phi}_{(\mathbf{K}-1)\mathbf{K}} \end{bmatrix} &= \begin{bmatrix} \mathbf{H}_{12} \\ \mathbf{H}_{23} \\ \vdots \\ \mathbf{H}_{(\mathbf{K}-1)\mathbf{K}} \end{bmatrix} \mathbf{\Delta p_{TR}} \end{aligned} \tag{28}$$

Genetic algorithm can be used to solve this problem [25].

$$\begin{gathered} \min_{\mathbf{\Delta p_{TR}}}\max\left(\mathbb{D}\left\{\mathbf{H}_{(k-1)k}\mathbf{\Delta p_{TR}} - \mathbf{\Delta\Phi}_{(k-1)k}\right\}\Big|_{k\in(1,\mathbf{K}-1)}\right) \\ s.t.\ |\mathbf{\Delta p_{TR}}| < \mathbf{d} \end{gathered} \tag{29}$$

where $\mathbf{d}$ is the error upper-bound. Matrix $\mathbf{L}$ is denoted to be equal to $\mathbf{H\Delta p_{TR}} - \mathbf{\Delta\Phi}$, and its k_{th} column vector is $\mathbf{H}_{(k-1)k}\mathbf{\Delta p_{TR}} - \mathbf{\Delta\Phi}_{(k-1)k}$. $\mathbb{D}\{\}$ is the function utilized to calculate the second-order norm between any two column vectors of the matrix $\mathbf{L}$. The phase residual with the GA is defined as

$$\varphi_{res}(i) = \frac{1}{2}(\max(\mathbf{L}(i,:)) + \min(\mathbf{L}(i,:))) \tag{30}$$

where $\mathbf{L}(i,:)$ is the ith row vector of the matrix $\mathbf{L}$.

Above all, the amplitude and delay errors in (4) can be calibrated by (22) and (23). The exact element positions are estimated by (29). After, the channel peak phases of a single target can be calibrated toward the ideal value, and the spatial phase residuals are small enough. Finally, the whole scene can be imaged by the BP algorithm after the inter-channel and element position error calibration.

4. Simulation and Experiment

4.1. Simulation Analysis

To verify the correctness of the proposed method, a simulation is performed. With the system parameters shown in Table 1, a FMCW (frequency modulated continuous wave) MIMO radar array with 16 TEs and 32 REs is used, as shown in Figure 4. Inter-channel errors and element position errors are added on the echo signal, where the amplitude, phase and element position errors are $A_{T,m}, A_{R,n} \sim U(0.25, 1)$, $\phi_{T,m}, \phi_{R,n} \sim U(-\pi, \pi)$ and $\Delta x_{T,m}, \Delta y_{T,m}, \Delta x_{R,n}, \Delta y_{R,n} \sim U(-3\ \text{mm}, 3\ \text{mm})$, respectively. U denotes the normal distribution. Four ideal targets T1 to T4 are utilized, and Table 2 shows their coordinates. The echo signals are with a SNR of -5 dB before pulse compression.

Table 1. System parameters for MIMO radar simulation.

Parameter	Value	Parameter	Value
Central Freq.	16.2 GHz	TEs Num.	16
Pulse Width	0.5 ms	REs Num.	32
Bandwidth	1 GHz	TEs interval	9.3 mm
Sample rate	100 MHz [1]	REs interval	74.4 mm

[1] Dechirp processing is used for FMCW signal.

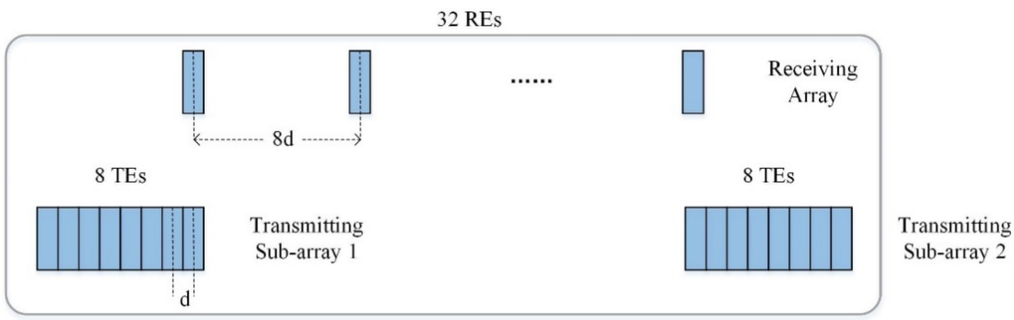

Figure 4. MIMO array with 16 TEs and 32 TEs.

Table 2. Prominent target positions in simulation.

Index	Range/m	Azimuth/deg
T1	2990	−30
T2	3000	0
T3	3010	30
T4	3020	15

With the BP algorithm, the echo signals are processed. Without error compensation, the focus performance of T4 is relatively bad, as shown in Figure 5a. A compensation method based on one single prominent target proposed in [19] is utilized to estimate the inter-channel amplitude and phase errors, as shown in Figure 5b. Two-dimensional profiles of T4 are shown in Figure 6. It can be noted that although the single-point calibration method can improve the overall imaging performance, the level of side-lobe is not good enough, which is mainly caused by the element position error.

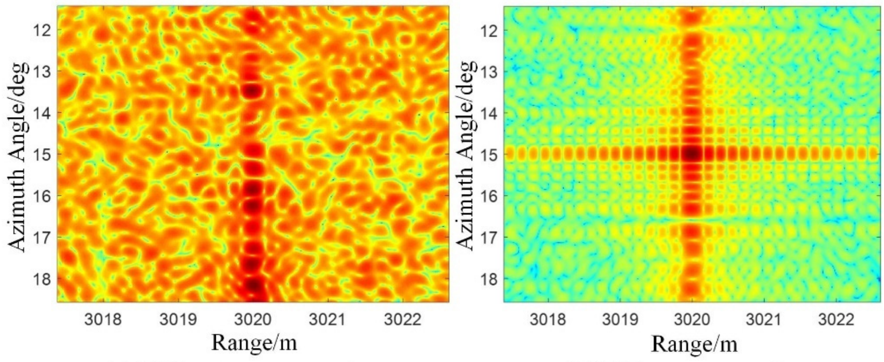

(a) Without compensation (b) With compensation

Figure 5. BP image result after conventional calibration (**a**) without compensation (**b**) with compensation.

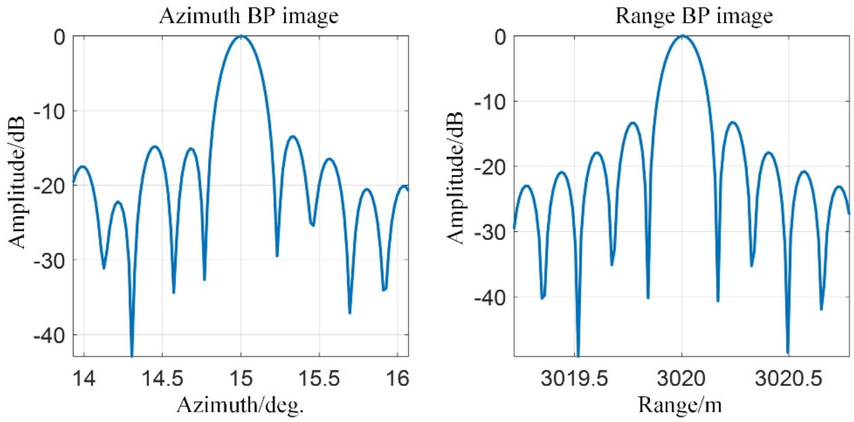

Figure 6. 2D profile of T4 after conventional calibration.

With the proposed method, the inter-channel errors and the element position errors are estimated. Figure 7a shows the estimated and actual element position errors. It is obvious that the proposed method can accurately estimate the element position error. After compensating the array errors, T4 is refocused and shown in Figure 7b. Figure 8 shows its two-dimensional profiles along the range and azimuth directions. The image performance, especially azimuth side-lobe performance, has been well improved after compensating the element position errors, which validates the effectiveness of the proposed method.

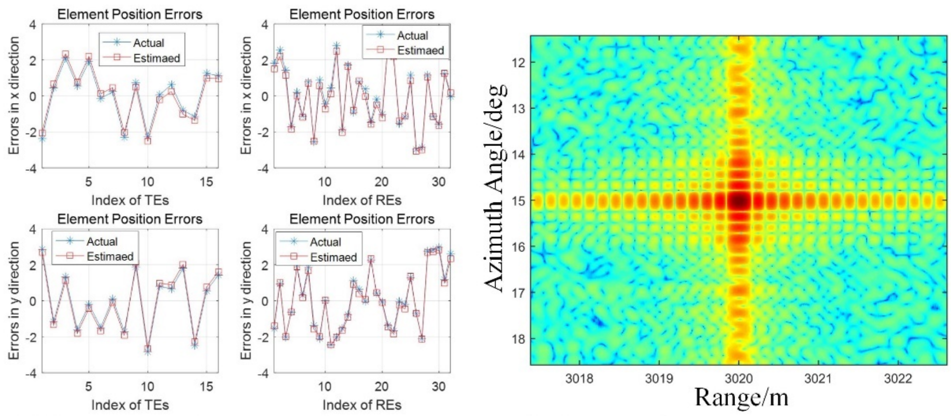

(a) Element position estimation accuracy (b) Image after error compensation

Figure 7. BP image result after element position error estimation and compensation (**a**) element position estimation accuracy; (**b**) image after error compensation.

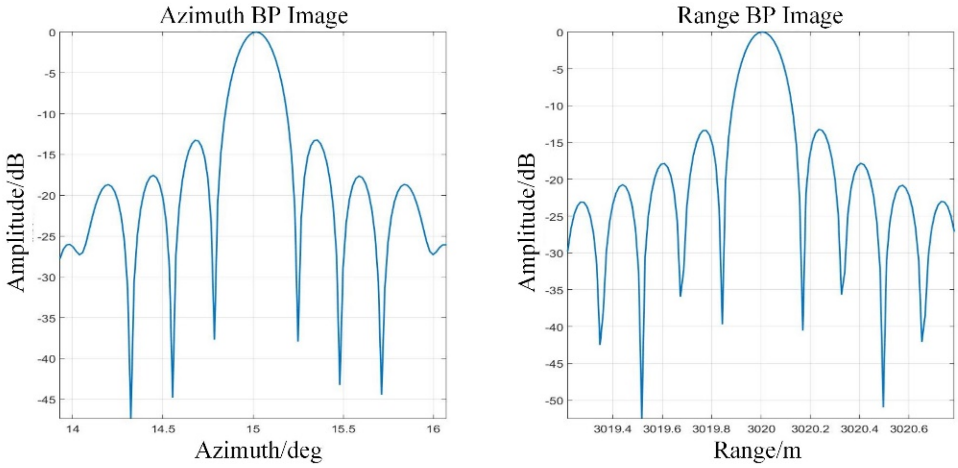

Figure 8. 2D profile of T4 after proposed calibration.

4.2. Experiment Analysis

As shown in Figure 9, a MIMO imaging radar is used in this experiment, whose array consists of two transmitting sub-arrays each with eight TEs (marked by two red boxes) and a receiving array with 32 REs (marked by a white box).

Figure 9. MIMO system utilized in the experiment.

The key parameters of the MIMO radar are shown in Table 3, and the experimental scene is a rocky slope as shown in Figure 10. Three transponders are utilized as the prominent points which are marked with circles, respectively recorded as T1, T2, and T3.

Table 3. System parameters.

Parameter	Value	Parameter	Value
Central Freq.	16.2 GHz	TEs Num.	16
Pulse Width	2 ms	REs Num.	32
Bandwidth	400 MHz	TEs interval	9.3 mm
Sample rate	12.5 MHz	REs interval	74.4 mm

Figure 11a shows the radar image without error compensation. Taking T3 as the reference target, the single point method (SPM) in [19] is utilized to compensate the inter-channel amplitude and phase errors, as shown in Figure 11b. With T1, T2 and T3 as the prominent targets, the proposed multi-point calibration method (MPM) is utilized to compensate both the element position and inter-channel errors, as shown in Figure 11c. Lastly, a self-calibration method, i.e., minimum-entropy autofocus (MEA) [26], is utilized, as shown in Figure 11d. It can be noted that the imaging performances have all been improved with the three calibration methods above.

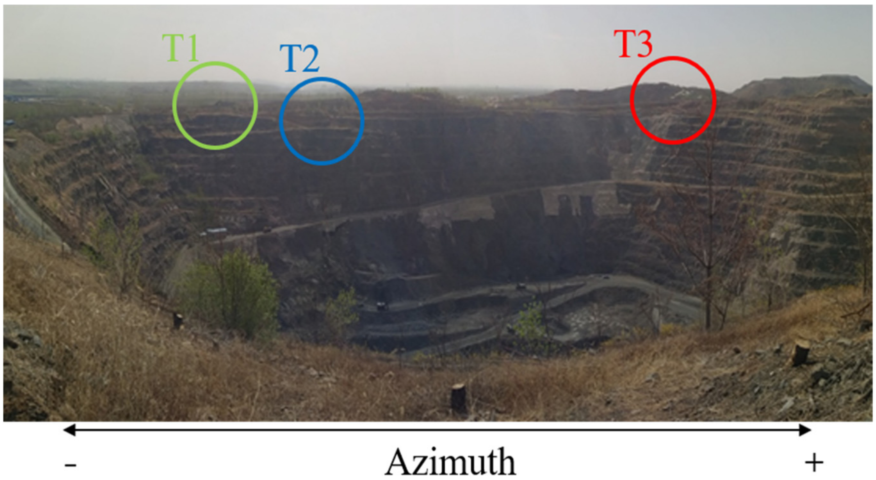

Figure 10. The scene of the experiment.

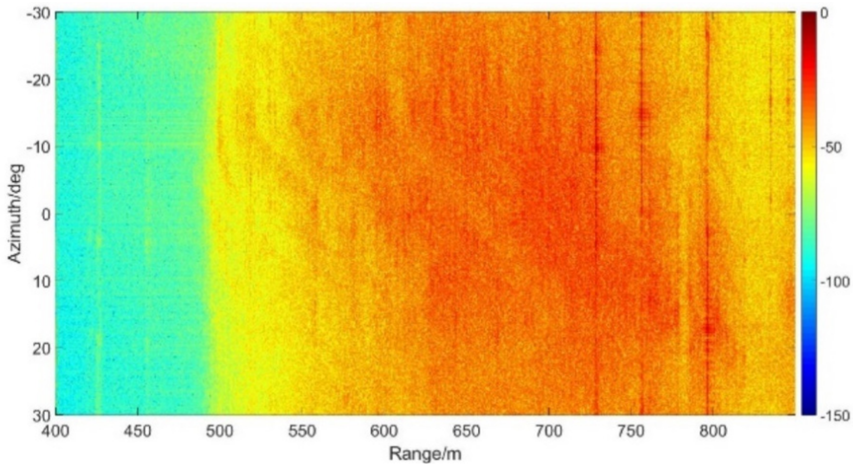

(**a**) Without Calibration

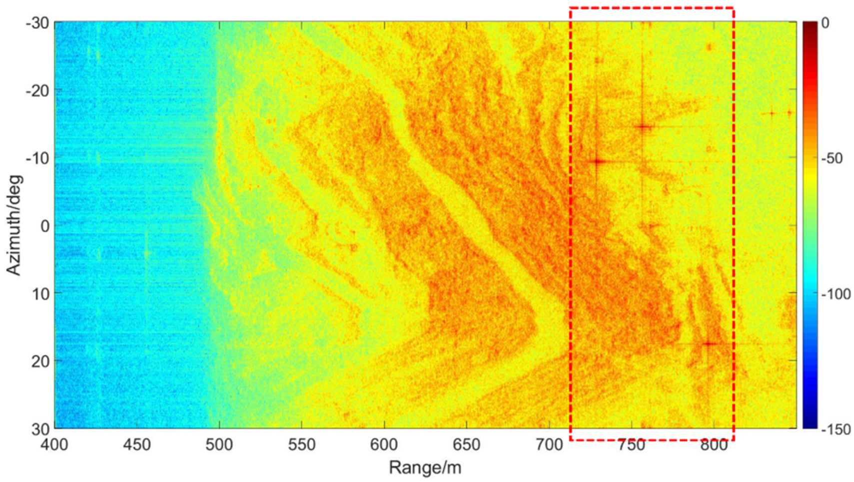

(**b**) SPM

Figure 11. *Cont.*

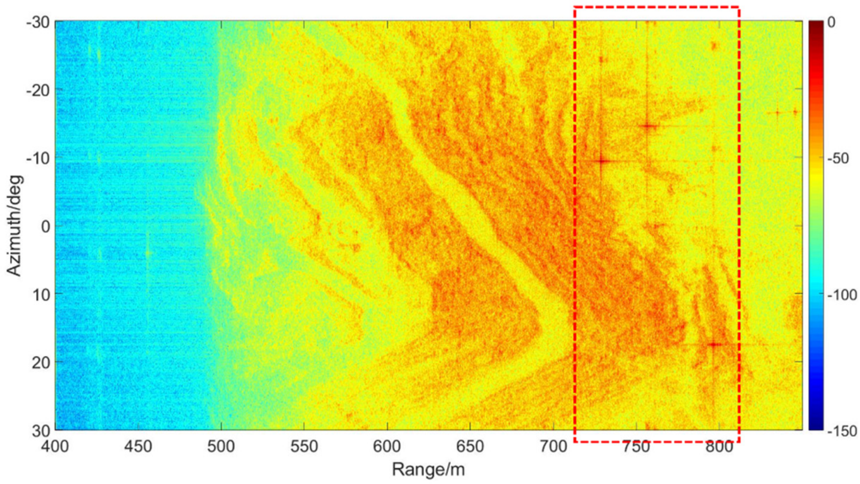

(**c**) MPM

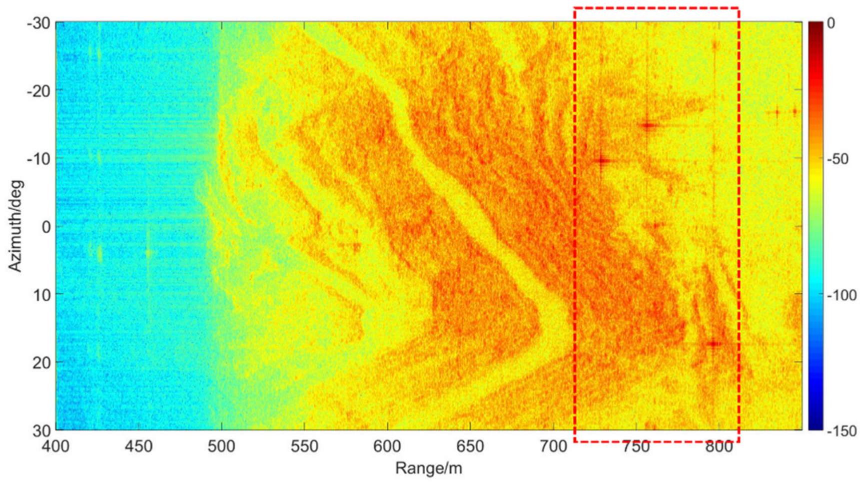

(**d**) MEA

Figure 11. Radar images with different calibration methods (**a**) without calibration (**b**) SPM (**c**) MPM (**d**) MEA.

To quantitively evaluate the imaging performances, T2 and T3 are utilized. Two active calibration methods, i.e., SPM and MPM, are firstly compared, as shown in Figure 12. For T3, the imaging performances of its range and azimuth profiles are almost the same with both methods. SPM method performs even better since it can calibrate T3 into an ideal point target. However, the SPM method cannot simultaneously compensate T2 and T3 because of the spatial variation of the element position error. For T2, with the MPM, its PSLR (peak sidelobe ratio) decreases from -11.33 dB to -12.99 dB, and the symmetry of side-lobes also increase.

In addition, it should be noted that the azimuths of T2 and T3 are slightly different of about 0.1° with both methods. The target location estimation with the SPM only depends on the channel's range information of a single target, while the MPM method utilizes all three targets, and increases the angle estimation accuracy with phase information. Theoretically, the MPM method could provide a more robust estimation performance.

The profiles of T2 with the MEA method is shown in Figure 13. Since the MEA method aims at improving the overall image performance rather than compensating based on one or multiple specific targets, the radar image can be significantly improved for Figure 11d contrast with Figure 11a. However, the profile of some specific targets, especially strong point targets, are sacrificed during the MEA iteration, which causes an azimuth envelope distortion in Figure 13.

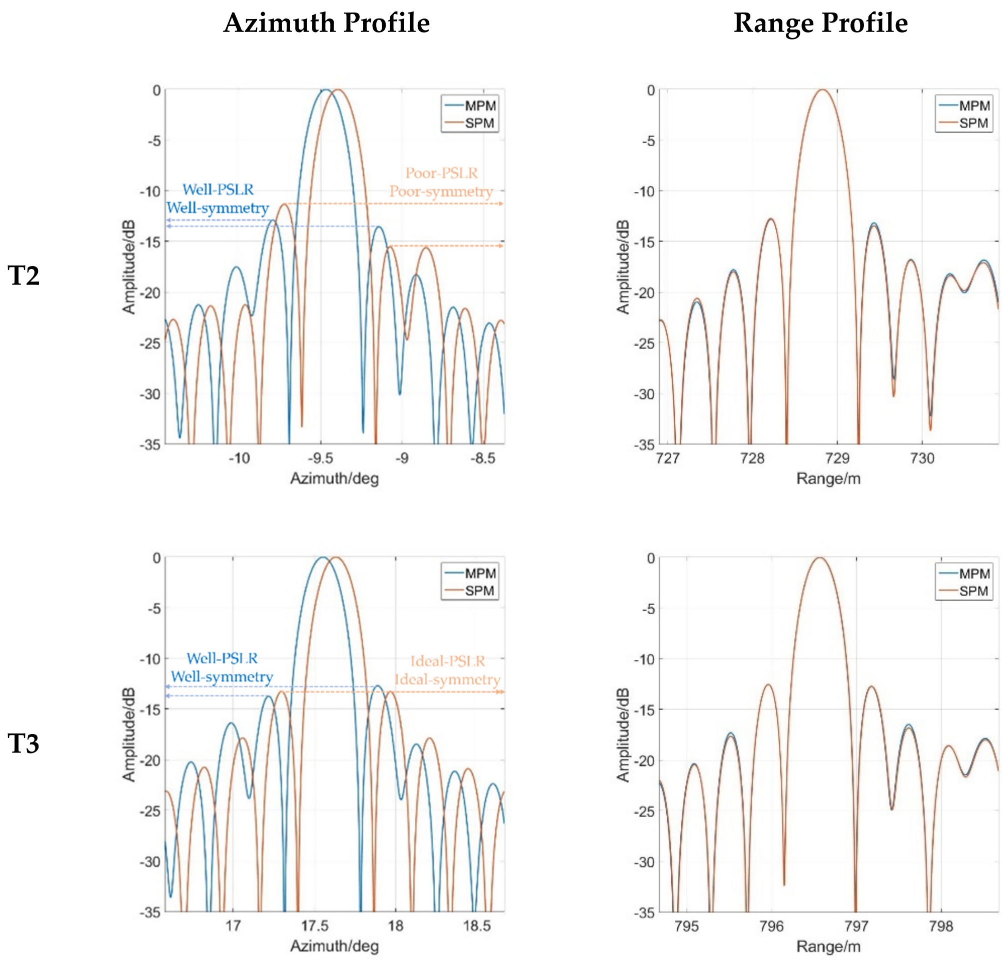

Figure 12. Targets' profiles with two active calibration methods.

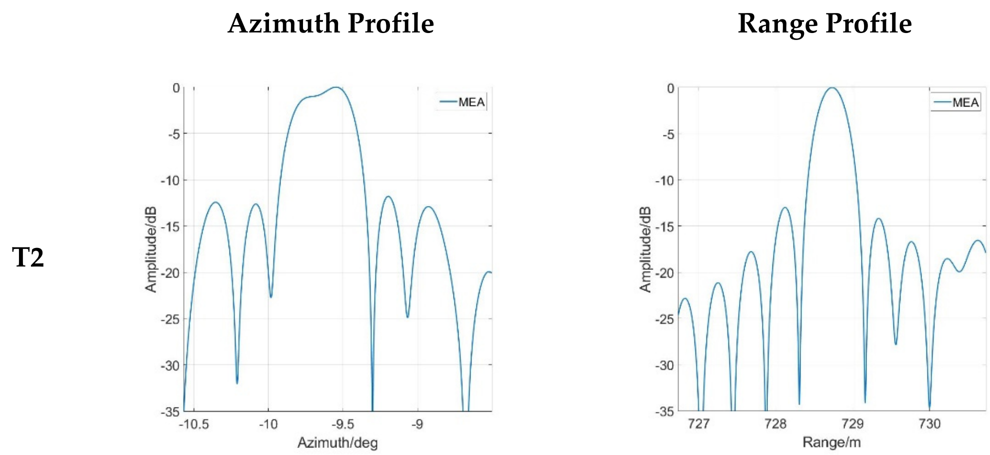

Figure 13. Target profile of self-calibration method.

5. Discussion

GB-MIMO's imaging performance is severely affected by array errors. The conventional methods, such as SPM and MEA in Section 4, cannot achieve good estimation in both wide-coverage and high-precision. Aiming at estimating both inter-channel errors and element position errors, an improved calibration method based on multi-prominent targets has been proposed.

The proposed method separates the inter-channel and element positions error with at least three prominent targets. The simulation in Figure 7 shows that the estimation accuracy of the element position could reach 0.5 mm level. The target's azimuth profile performance in Figure 8, including PSLR and side-lobe symmetry, has been much improved from Figure 6.

Utilizing different calibration methods, four radar images of a rocky slope are shown in Figure 11. The comparison is summarized in Table 4. The results show that all the calibration methods have increased the image quality. The MPM could achieve the best azimuth PSLR and the smallest image entropy, which reach −12.99 dB and 11.77, respectively. The SPM can achieve an ideal PSLR for T3 at −13.2 dB, but the PSLR and side-lobe symmetry for T2 are worse than those with the MPM method. With the MEA method, the azimuth profile of the prominent target is distorted, but it can effectively decrease the image entropy from the original level of 13.13 to 11.95, and can be operated in any situation without any reference target.

Table 4. Comparison of different calibration methods.

	SPM	**MPM**	**MEA**
Azimuth PSLR	−11.33 dB	−12.99 dB	−11.80 dB
Image Entropy	11.80	11.77	11.95 (Ori. 13.13)
Calibration Time	20 s	10 min	>5 h
Pros.	Easy & Fast	Spatial-variant Elimination	Without Reference

6. Conclusions

This paper proposed a method of estimating and compensating the array errors based on multiple prominent targets. Firstly, target positions are robustly estimated. Secondly, the amplitude and delay errors are estimated based on ECLS. Finally, in order to compensate the spatial-varying phase error, the element position errors are extracted and estimated based on the channel-cancelation and GA, respectively.

Both simulated and experimental datasets have validated the correctness and effectiveness of the proposed calibration method based on multiple prominent targets. The estimation accuracy of the element positions can reach millimeter level. Besides, the image calibrated by the proposed method achieves the best PSLR at −12.99 dB and the smallest image entropy at 11.77 compared with two conventional methods.

Author Contributions: Conceptualization, Z.Z. and W.T.; methodology, Z.Z.; validation, Y.D.; formal analysis, Z.Z.; investigation, C.H.; resources, W.T.; data curation, Y.D.; writing—original draft preparation, Z.Z.; writing—review and editing, Y.D.; visualization, C.H.; supervision, T.Z.; project administration, W.T.; funding acquisition, C.H. and T.Z. All authors have read and agreed to the published version of the manuscript.

Funding: This work was funded in part by the National Natural Science Foundation of China under Grants 61971037, 61960206009, and 31727901, and in part by the Natural Science Foundation of Chongqing, China, under Grants cstc2020jcyj-jqX0008 and cstc2020jcyj-msxmX0608.

Institutional Review Board Statement: Not applicable.

Informed Consent Statement: Not applicable.

Conflicts of Interest: The authors declare no conflict of interest.

References

1. Pieraccini, M.; Miccinesi, L. Ground-based radar interferometry: A bibliographic review. *Remote Sens.* **2019**, *11*, 1029. [CrossRef]
2. Hu, C.; Zhu, M. High-Precision deformation monitoring algorithm for GBSAR system: Rail de-termination phase error compensation. *Sci. China Inf. Sci.* **2015**, *58*, 082307. [CrossRef]

3. Tian, W.; Li, Y. Vibration Measurement Method for Artificial Structure Based on MIMO Imaging Radar. *IEEE Trans. Aerosp. Electron. Syst.* **2020**, *56*, 748–760. [CrossRef]
4. Deng, Y.; Hu, C. A Grid Partition Method for Atmospheric Phase Compensation in GB-SAR. *IEEE Trans. Geosci. Remote Sens.* **2021**, 1–13. [CrossRef]
5. Tarchi, D.; Oliveri, F. MIMO Radar and Ground-Based SAR Imaging Systems: Equivalent Approaches for Remote Sensing. *IEEE Trans. Geosci. Remote Sens.* **2013**, *51*, 425–435. [CrossRef]
6. Wang, H. *MIMO Radar Imaging Algorithms*; National University of Defence Technology: Changsha, China, 2010.
7. Jia, Y.; Bao, Z. A new calibration technique with signal sources for position, gain and phase uncertainty of sensor array. *Acta Electron. Sin.* **1996**, *24*, 47–52.
8. Sheng, G.; Wang, H. Fast Angle Estimation and Sensor Self-Calibration in Bistatic MIMO Radar with Gain-Phase Errors and Spatially Colored Noise. *IEEE Access* **2020**, *8*, 123701–123710. [CrossRef]
9. Xu, X.; Zhou, X. Radar coincidence imaging with array position error. In Proceedings of the IEEE International Conference on Signal Processing, Communications and Computing (ICSPCC), Ningbo, China, 19–22 September 2015; Institute of Electrical and Electronics Engineers: Piscataway, NJ, USA, 2015; pp. 1–4.
10. Yang, J.; Huang, X. Compressed Sensing Radar Imaging with Compensation of Observation Position Error. *IEEE Trans. Geosci. Remote Sens.* **2014**, *52*, 4608–4620. [CrossRef]
11. Gumbmann, F.; Schmidt, L.P. Millimeter-Wave Imaging with Optimized Sparse Periodic Array for Short-Range Applications. *IEEE Trans. Geosci. Remote Sens.* **2011**, *49*, 3629–3638. [CrossRef]
12. Solomon, I.; Gray, D. Receiver Array Calibration Using Disparate Sources. *IEEE Trans. Antennas Propag.* **1999**, *47*, 496–505. [CrossRef]
13. Liu, C.; Yan, J. Sparse self-calibration by map method for MIMO radar imaging. In Proceedings of the IEEE International Conference on Acoustics, Speech and Signal Processing (ICASSP), Kyoto, Japan, 25–30 March 2012; Institute of Electrical and Electronics Engineers: Piscataway, NJ, USA, 2012; pp. 2469–2472.
14. Sammartin, P.; Tarchi, D. Phase compensation and processing in multiple-input–multiple-output radars. *IET Radar Sonar Navig.* **2012**, *6*, 222–232. [CrossRef]
15. Ma, Z.; Liu, Y. Sparse recovery-based space-time adaptive processing with array error self-calibration. *Electron. Lett.* **2014**, *50*, 952–954. [CrossRef]
16. Kim, J.; Yang, H. Blind Calibration for a Linear Array with Gain and Phase Error Using Independent Component Analysis. *IEEE Antennas Wirel. Propag. Lett.* **2010**, *9*, 1259–1262. [CrossRef]
17. Wylie, M.; Roy, S. Joint DOA estimation and phase calibration of linear equispaced (LES) arrays. *IEEE Trans. Signal Process.* **1994**, *42*, 3449–3459. [CrossRef]
18. Huo, R.; Tian, W. A compensation method of multiple-channel amplitude and phase errors for MIMO imaging radar. *J. Eng.* **2019**, *19*, 5901–5904. [CrossRef]
19. Schmid, C.; Pfeffer, C. An FMCW MIMO radar calibration and mutual coupling compensation approach. In Proceedings of the 2013 European Radar Conference, Nuremberg, Germany, 9–11 October 2013; Institute of Electrical and Electronics Engineers: Piscataway, NJ, USA, 2013; pp. 13–16.
20. Liu, Y.; Xu, X. MIMO Radar Calibration and Imagery for Near-Field Scattering Diagnosis. *IEEE Trans. Aerosp. Electron. Syst.* **2018**, *54*, 442–452. [CrossRef]
21. Zeng, T.; Mao, C. Ground-based SAR wide view angle full field imaging algorithm based on keystone formatting. *IEEE JSTARS* **2016**, *9*, 2160–2170. [CrossRef]
22. Hu, C.; Wang, J. Generalized Ambiguity Function Properties of Ground-Based Wideband MIMO Imaging Radar. *IEEE Trans. Aerosp. Electron. Syst.* **2019**, *55*, 578–591. [CrossRef]
23. Hu, C.; Wang, J. Design and Imaging of Ground-Based Multiple-Input Multiple-Output Synthetic Aperture Radar with Non-Collinear Arrays. *Sensors* **2017**, *17*, 598. [CrossRef] [PubMed]
24. Wei, M. *Theory and Calculation of Generalized Least Squares Problem*; Science Press: Beijing, China, 2006.
25. Koza, J. *Genetic Programming*; MIT Press: Cambridge, MA, USA, 1992.
26. Zeng, T.; Wang, R. SAR image autofocus utilizing minimum-entropy criterion. *IEEE GRSL* **2013**, *10*, 1552–1556. [CrossRef]